

Cite this: *Dalton Trans.*, 2024, **53**,
2008

Synergistic optimization of triple phase junctions and oxygen vacancies over $\text{Mn}_x\text{Cd}_{1-x}\text{S}/\text{Ov}-\text{WO}_3$ for boosting photocatalytic hydrogen evolution†

Haitao Zhao, *^a Hongjie Zhu, ^a Min Wang,^a Heyuan Liu ^b and Xiyou Li *^c

Strengthening the separation of photogenerated charge carriers is crucial for improving the efficiency of photocatalytic hydrogen evolution. Herein, $\text{t-Mn}_{0.5}\text{Cd}_{0.5}\text{S}/\text{Ov}-\text{WO}_3$ (t-MCSW) triple-phase junctions with rich oxygen vacancies were developed using the calcination-hydrothermal method. The corresponding morphology and structure of the samples were examined by XRD, TEM and XPS. The formation of the S-scheme heterostructure in t-MCSW has also been confirmed with *in situ* XPS, work function analysis and free radical capture tests. The experimental results demonstrate that t-MCSW-7 exhibited optimal activity ($194.2 \text{ mmol g}^{-1} \text{ h}^{-1}$), which was about 4 times higher than that of the individual $\text{Mn}_{0.5}\text{Cd}_{0.5}\text{S}$ (t-MCS, $48.8 \text{ mmol g}^{-1} \text{ h}^{-1}$). The apparent quantum yield of t-MCSW-7 is 29.14% at 420 nm, and the material exhibits excellent stability after seven cycles of photocatalytic reaction. The excellent photocatalytic activity of t-MCSW-7 is attributed to more efficient separation of charge carriers by triple-phase junctions connected by homojunctions and heterojunctions. Moreover, the existence of oxygen vacancies broadens absorption spectra and accelerates surface charge transfer. The synergistic effect of phase junctions and oxygen vacancies leads to an enhancement of hydrogen evolution activity. This work provides a new idea for preparing efficient photocatalysts.

Received 8th December 2023,
Accepted 30th December 2023

DOI: 10.1039/d3dt04104b

rsc.li/dalton

1. Introduction

Hydrogen has garnered widespread attention due to its high energy density, convenient storage, and pollution-free combustion.^{1–5} The utilization of semiconductor-based photocatalytic water splitting to generate hydrogen gas from inexhaustible solar energy is a viable solution to achieve carbon neutrality.^{6,7} In the domain of photocatalytic hydrogen production, sulfide-based semiconductors have been extensively explored as the most typical photocatalysts, including CdS,^{6,8} CdIn_2S_4 ,^{2,9} $\text{Zn}_x\text{Cd}_{1-x}\text{S}$,^{10–13} and $\text{Mn}_x\text{Cd}_{1-x}\text{S}$.^{14–17} Among these photocatalysts, the $\text{Mn}_x\text{Cd}_{1-x}\text{S}$ solid solution has led to a new wave of interest, owing to its adjustable band energy structure by adjusting the ratio of x -components, strong redox potentials, and effective light response.^{18–21} Although $\text{Mn}_x\text{Cd}_{1-x}\text{S}$

possesses great potential for photocatalytic hydrogen evolution, it also has some disadvantages such as fast recombination of photogenerated charge carriers and easy photo-corrosion.

The combination of different crystal phases or semiconductors enables the promotion of the rapid transfer of photogenerated electron-hole pairs within the system, prolonging the lifetime of charge carriers, leading to the enhancement of the photoelectric conversion effect. The formation of a homojunction between two crystal phases in a material can accelerate the carrier separation, which is attributed to the built-in electric field across the junction.^{22,23} Wang *et al.* first reported a twin $\text{Mn}_x\text{Cd}_{1-x}\text{S}$ containing the WZ and ZB phases prepared using a one-pot solvothermal process, where the photocatalytic hydrogen activity reached $61.4 \text{ mmol g}^{-1} \text{ h}^{-1}$.²⁴ In order to further improve the H_2 efficiency of the single twin $\text{Mn}_x\text{Cd}_{1-x}\text{S}$ photocatalyst, researchers proposed building heterojunctions. Heterojunctions formed by different semiconductors can achieve a spatial separation of electrons. Electrons driven by the heterojunction interface are transferred to different material surfaces for catalytic reactions.^{25–31} For instance, Zhao *et al.* reported that the hydrogen evolution rate of $\text{Ni}_{12}\text{P}_5/\text{T-Mn}_{0.5}\text{Cd}_{0.5}\text{S}$ is $96.5 \text{ mmol g}^{-1} \text{ h}^{-1}$.³² Liu *et al.* have reported $\text{NiP}_x/\text{T-Mn}_{0.5}\text{Cd}_{0.5}\text{S}$ heterojunction composites with a high H_2 evolution rate.³³ Lv *et al.* prepared MoO_2/Au

^aShandong Provincial Key Laboratory of Chemical Energy Storage and Novel Cell Technology, School of Chemistry and Chemical Engineering, Liaocheng University, Liaocheng, 252059, China. E-mail: zhaohaitao_2014@163.com

^bCollege of New Energy, China University of Petroleum (East China), Qingdao, Shandong, 266580, China

^cSchool of Materials Science and Engineering, China University of Petroleum (East China), Qingdao, Shandong, 266580, China. E-mail: xiyouli@upc.edu.cn

† Electronic supplementary information (ESI) available. See DOI: <https://doi.org/10.1039/d3dt04104b>

T-Mn_{0.5}Cd_{0.5}S multiple heterojunctions with significant hydrogen evolution activity compared to pristine twin Mn_{0.5}Cd_{0.5}S.³⁴ Nonetheless, compared with homojunctions, heterojunctions exhibit slower transfer of photoinduced charge carriers due to lattice mismatches and poor interfacial contact. If two types of junctions exist simultaneously, it is necessary to regulate the surface carrier transfer rate of the heterojunction to achieve a match with the electron transfer efficiency of the homojunction.

To achieve the above purpose, surface vacancy engineering is considered an effective strategy. The effective introduction of oxygen vacancies on the surface of the metal oxide can effectively accumulate photogenerated electrons and expedite electron transfer.³⁵ WO₃ exhibits a narrow band gap of 2.4–2.7 eV, a high oxidation potential of 3.49 eV vs. SHE and notable chemical stability.^{36–38} At the present time, various morphologies of WO₃ have been prepared.^{39–42} During the preparation process, oxygen vacancies appear on the surface of WO₃.^{1,43} Inspired by this, we propose to combine rich oxygen vacancies in WO₃ (Ov-WO₃) with the Mn_{0.5}Cd_{0.5}S homojunction to form a heterojunction, and to use oxygen vacancies to inject more photogenerated electrons into the Mn_{0.5}Cd_{0.5}S homojunction, further ensuring the stability of photogenerated electrons on the surface of photocatalysts and improving hydrogen evolution activity.

In this paper, we synthesized a novel Mn_{0.5}Cd_{0.5}S/Ov-WO₃ (t-MCSW-*x*) triple-phase junction with rich oxygen vacancies using a simple hydrothermal method. On the one hand, the lifetime of photogenerated carriers can be prolonged by combining homojunctions and heterojunctions. On the other hand, the introduction of oxygen vacancies improves the electron transfer rate on the heterojunction interface, while the oxygen vacancies as an electron pool inject electrons into the homojunction to maintain the electronic stability of the t-MCSW system. Therefore, on the introduction of an Ov-WO₃ mass fraction of 7 wt%, the hydrogen production activity of the t-Mn_{0.5}Cd_{0.5}S/Ov-WO₃-7 wt% (t-MCSW-7) composite material becomes as high as 194.2 mmol g⁻¹ h⁻¹, which is 4 times higher than that of pristine t-MCS. The work provides a new perspective on the preparation of efficient and photo-stable photocatalysts.

2. Experimental

2.1. Preparation of Ov-WO₃ nanosheets

Ov-WO₃ nanosheets were prepared using the hydrothermal and high-temperature calcination procedure. Initially, 1 g of sodium tungstate dihydrate (Na₂WO₄·2H₂O) and 0.6 g of citric acid (C₆H₈O₇) were mixed in 70 mL of deionized water and stirred for 30 minutes. Afterwards, the pH of the mixture was regulated to around 1 with 6 M HCl, forming a yellow precipitate. Then, the suspension was transferred to a 100 mL Teflon-lined autoclave and maintained at 120 °C for 12 h. The resulting sample was centrifuged and dried at 70 °C for 12 h and the product was named WO₃. 600 mg of the WO₃ sample was cal-

cined at a rate of 5 °C per minute to 500 °C and maintained for 2 h in a muffle furnace. The final product was marked as Ov-WO₃.

2.2. Synthesis of Mn_{0.5}Cd_{0.5}S/Ov-WO₃ (t-MCSW-*x*) nanocomposites

Mn_{0.5}Cd_{0.5}S/Ov-WO₃ (t-MCSW-*x*) nanocomposites were prepared *via* an *in situ* one-pot hydrothermal method. Firstly, 5 mmol of Mn(CH₃COO)₂·4H₂O, 5 mmol of Cd(CH₃COO)₂·2H₂O and 13 mmol of thioacetamide (TAA) were mixed with 60 mL of deionized water under stirring for 1 h. Subsequently, 5 mL of 4 M NaOH was added to the mixture under constant stirring for 1 h. Then, different quantities of Ov-WO₃ nanosheets were added to the above solution and stirred fully for 30 minutes. The solutions were transferred to a 100 mL Teflon-lined autoclave and heated at 160 °C for 24 h. After completion of the reaction, the samples were centrifuged five times with water and ethanol and dried at 80 °C overnight. The mass fractions (wt%) of Ov-WO₃ added to Mn_{0.5}Cd_{0.5}S (t-MCS) were 0%, 1%, 3%, 5%, 7%, and 10%, respectively. The resulting nanocomposites were denoted as t-MCS, t-MCSW-1, t-MCSW-3, t-MCSW-5, t-MCSW-7, and t-MCSW-10.

In addition, the hydrothermal method described above was utilized to prepare a series of nanotwin Mn_{*x*}Cd_{1-*x*}S samples without the introduction of Ov-WO₃ sheets. The process involved using *x* mmol of Mn(CH₃COO)₂·4H₂O and 1-*x* mmol of Cd(CH₃COO)₂·2H₂O as precursor materials. The final products were marked as CdS, Mn_{0.2}Cd_{0.8}S, Mn_{0.3}Cd_{0.7}S, Mn_{0.5}Cd_{0.5}S (t-MCS), Mn_{0.7}Cd_{0.3}S, Mn_{0.8}Cd_{0.2}S and MnS when the mole amounts of *x* were 0, 0.2, 0.3, 0.5, 0.7, 0.8 and 1.0, respectively.

2.3. Photocatalytic H₂ production experiment

To evaluate the photocatalytic hydrogen evolution activity, 10 mg of the photocatalyst was dispersed in 100 mL of 0.25 M Na₂S and 0.35 M Na₂SO₃ sacrificial agents, in a Pyrex glass system equipped with a 300W Xe lamp (CEL-SPH2N) with a UV-cutoff filter ($\lambda \geq 420$ nm). This system was linked to a GC 7900 online gas chromatograph with a TCD detector. A more detailed process for the photocatalytic evaluation and calculation of the apparent quantum yield (AQY) can be found in the ESI.†

3. Results and discussion

3.1. Typical structure and morphology analysis

X-ray diffraction (XRD) was utilized to characterize the crystal structure and phase composition of the materials. As shown in Fig. 1a, the characteristic peaks of the as-prepared Ov-WO₃ are located at 23.08°, 23.67°, 24.10°, 33.19° and 34.14° corresponding to the (001), (020), (200), (021) and (220) planes of WO₃ (PDF#20-1324), respectively.⁴⁰ XRD patterns of a series of Mn_{*x*}Cd_{1-*x*}S are shown in Fig. 1b. Compared with the characteristic peak position of CdS, the peaks of Mn_{*x*}Cd_{1-*x*}S shift towards a higher angle with an increase in the Mn²⁺ molar

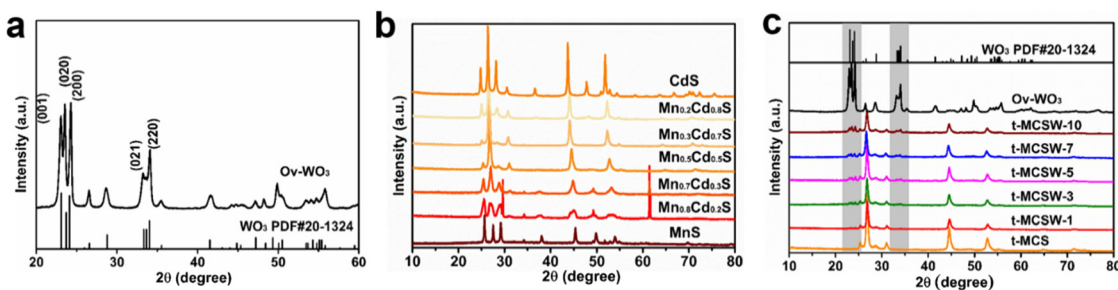


Fig. 1 Typical powder XRD diffraction patterns of (a) Ov-WO₃, (b) Mn_xCd_{1-x}S nanotwins, and (c) t-MCSW-*x*.

ratio.^{21,32,44} Compared with the peaks of CdS and MnS, the peaks of Mn_{0.5}Cd_{0.5}S exhibit a significant shift. This shift in the angle is a clear indication that the Mn_{0.5}Cd_{0.5}S solid solution has been successfully fabricated. In the EDS spectra (Fig. S1†), it is further confirmed that the molar ratio of Mn²⁺:Cd²⁺ is close to 1:1. Fig. S2† shows that peaks of Mn_{0.5}Cd_{0.5}S at 25.37°, 26.80°, 28.74°, 31.01°, 44.63° and 52.70° are assigned to the (100), (002), (101), (200), (220) and (311) crystal planes of CdS (PDF#41-1049, PDF#10-0454) and MnS (PDF#40-1289, PDF#06-0518), respectively.^{19,20,45,46} In addition, for the Mn_{0.8}Cd_{0.2}S material, characteristic peaks located at 31° and 62° corresponding to cubic MnS (PDF#06-0518) appear, suggesting that Mn_{0.8}Cd_{0.2}S is a mixture consisting of cubic MnS and Mn–Cd–S solid solution.¹⁹

Fig. 1c presents XRD patterns of the obtained t-Mn_{0.5}Cd_{0.5}S/Ov-WO_{3-x} (t-MCSW-*x*) composites. With the increase in the loading content of Ov-WO₃ in t-MCSW-*x* composites, the characteristic peaks of Ov-WO₃ become more prominent. Importantly, the introduction of Ov-WO₃ does not induce any disruption in the peaks of t-MCS. This observation suggests the nanocomposite is primarily composed of t-MCS and Ov-WO₃.

Scanning electron microscopy (SEM) and transmission electron microscopy (TEM) images were employed to assess the morphology of the samples. As shown in Fig. 2a, t-MCS contains non-uniform nanoparticles. Ov-WO₃ exhibits a nanosheet structure with a relatively small size and a thickness of about 20–30 nm (Fig. 2b, Fig. S3†). From Fig. 2c and d, it is easy to observe that t-MCS nanoparticles are loaded on Ov-WO₃ nanosheets in the t-MCSW-7 nanocomposite. Fig. S4† shows the high-resolution transmission electron microscopic (HRTEM) image of t-MCS. It can be clearly observed that the lattice fringes exhibit a staggered arrangement of the ZB phase and WZ phase of Mn_{0.5}Cd_{0.5}S, indicating the successful formation of nanotwin MCS.^{24,32,33} The homojunction interface between the ZB and WZ phases ensures fluent electron transfer, resulting in promoted photocatalytic activity. The HRTEM of t-MCSW-7 in Fig. 2e also clearly shows the interface between t-MCS and Ov-WO₃, marked with a red dashed line. The intimate contact interface demonstrates the formation of t-MCS and Ov-WO₃ heterojunctions. The lattice spacings of 0.312 nm and 0.332 nm belong to the t-MCS (002) and Ov-WO₃ (200)

crystal facets, respectively.³³ In addition, significant atomic defects can be observed in the Ov-WO₃ nanolattice, marked with a yellow dashed line, indicating the existence of oxygen vacancies in Ov-WO₃. Elemental mappings of the t-MCSW-7 composite photocatalyst show Mn, Cd, S, W, and O elements as presented in Fig. 2h–l. These results demonstrate the successful preparation of t-Mn_{0.5}Cd_{0.5}S/Ov-WO₃ (t-MCSW) triple-phase heterojunctions with oxygen vacancies.

X-ray photoelectron spectroscopy (XPS) was employed to examine elemental information and valence states of the surface of the samples, as well as to ascertain the direction of the electron migration at the interface of the t-MCSW-7 composite by analyzing the change in the binding energy. As illustrated in Fig. 3a, the survey spectrum of t-MCSW-7 detects elemental peaks of Mn, Cd, S, W, and O, which are consistent with the elemental mappings. For pristine t-MCS, the high-resolution XPS spectrum of Cd 3d displays two symmetrical peaks located at 404.44 eV and 411.2 eV, belonging to Cd 3d_{5/2} and Cd 3d_{3/2} of Cd²⁺, respectively (Fig. 3b).⁴⁷ In the Mn 2p XPS spectrum, three peaks at 640.7 eV, 651.8 eV, and 645.1 eV are attributed to Mn 2p_{3/2}, Mn 2p_{1/2} and a satellite peak of Mn²⁺, respectively (Fig. 3c).⁴⁶ S 2p peaks at approximately 160.86 eV and 162.00 eV correspond to S 2p_{3/2} and S 2p_{1/2} of S²⁻, respectively (Fig. 3d). For Ov-WO₃, W 4f peaks at 35.24 eV and 37.40 eV are assigned to W 4f_{7/2} and W 4f_{5/2} of W⁶⁺, respectively (Fig. 3e).^{37,39,43} In addition, in the O 1s XPS spectrum (Fig. 3f), the primary peak at about 530.06 eV corresponds to lattice oxides, while the binding energy at 531.79 eV is attributed to the oxygen vacancy.⁴⁸

Compared with pure t-MCS, the binding energy positions of Mn 2p, Cd 3d, and S 2p of t-MCSW-7 show a positive shift. Meanwhile, compared with pristine Ov-WO₃, peaks of W 4f and O 1s XPS spectra exhibit negative shifts in t-MCSW. The changes in the binding energies indicate the presence of strong interactions between t-MCS and Ov-WO₃ in the t-MCSW composite. An increase in the binding energy indicates a decrease in the electron cloud density, thus electrons drift from t-MCS to Ov-WO₃ in the composite. In addition, under irradiation, all peaks for t-MCSW-7 were observed to move in the opposite direction compared with that under dark conditions for further analysis of the electron transfer mechanism. In Fig. 4a, a strong EPR signal of the Ov-WO₃ nanosheet

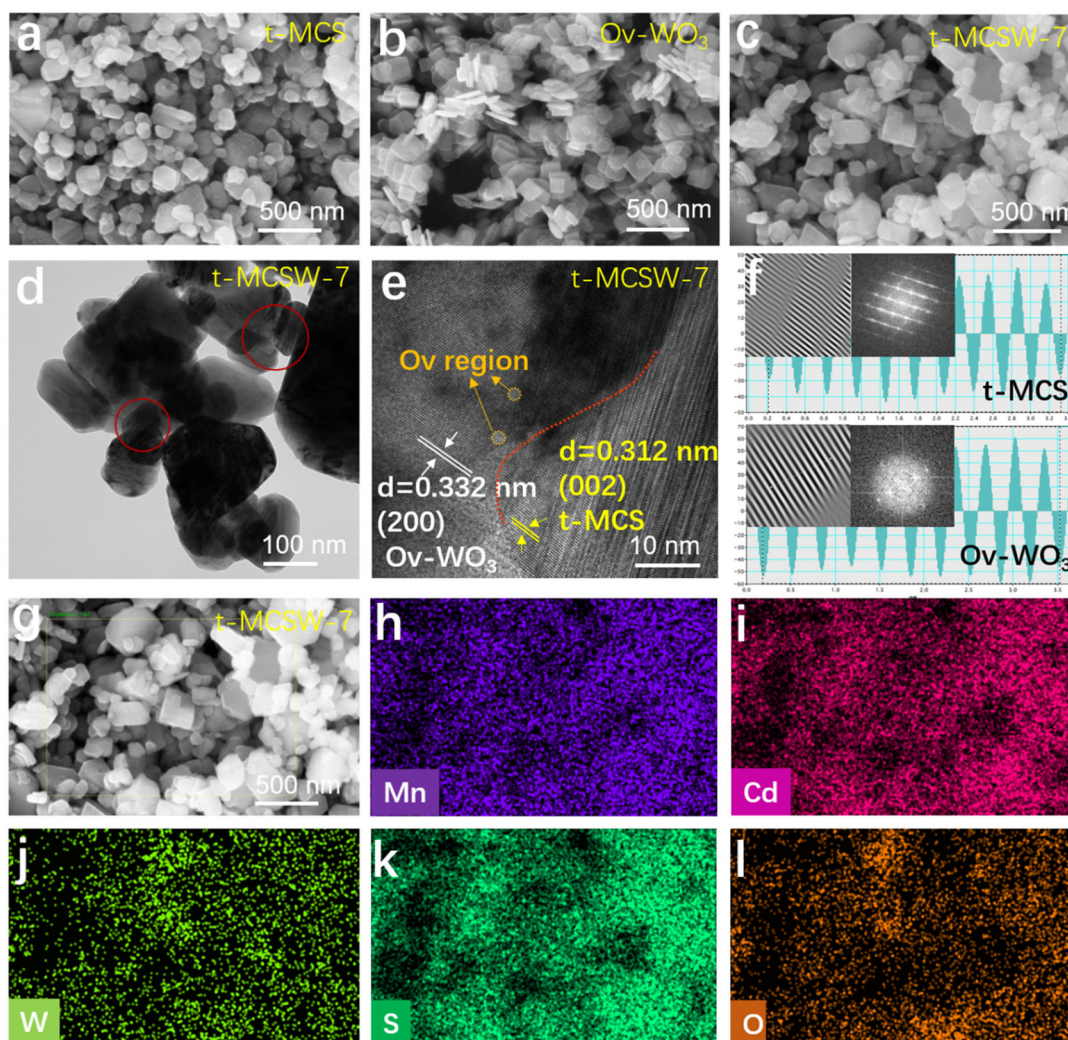


Fig. 2 SEM images of (a) t-MCS, (b) Ov-WO₃, (c) t-MCSW-7, (d) TEM, (e) HRTEM, (g) SEM, (h–l) and EDS elemental mapping images of Mn, Cd, S, W, and O elements.

is observed at a g value of 2.001, demonstrating the presence of surface oxygen vacancies compared to WO₃, which corresponds well with the XPS result. The above results prove that the t-MCSW heterojunction has been successfully prepared, while the presence of oxygen vacancies as electron capture centers enables the separation of photoinduced charge carriers and amplifies the interface electric field.⁴⁹

The N₂ adsorption–desorption isotherms and pore size distribution curves for Ov-WO₃, WO₃, t-MCS and t-MCSW-7 are displayed in Fig. 4b. Type IV isotherms and the H3 hysteresis loop demonstrate mesoporous samples. The corresponding surface area and pore sizes are presented in Table S1.† Compared with the surface area of WO₃ (11.95 m² g⁻¹), the Ov-WO₃ nanosheets have a large surface area of 34.62 m² g⁻¹. By adding Ov-WO₃ nanosheets, the specific surface area of t-MCSW-7 increases to 18.40 m² g⁻¹ compared to that of t-MCS (6.87 m² g⁻¹), indicating oxygen vacancies increase the specific

surface area and provide a number of reaction active sites for enhanced photocatalytic activity.

3.2. UV-vis diffuse reflection spectra

UV-vis diffuse reflection spectra (UV-vis DRS) represent the sample's optical absorption capacity. The absorption spectra of nanotwin Mn_xCd_{1-x}S solid solutions are shown in Fig. S5.† The absorption band edges were gradually blue-shifted as the Mn content increased, indicating that the bandgaps of the Mn_xCd_{1-x}S solid solution gradually increased compared to that of CdS. A suitable bandgap can effectively suppress the recombination of photoinduced carriers, helping to promote photocatalytic hydrogen evolution. As shown in Fig. 4c, compared to WO₃, the absorption band edge of Ov-WO₃ displays a red-shift and its optical intensity is notably improved between 500 and 800 nm after the introduction of oxygen vacancies. Notably, with the introduction of Ov-WO₃, the

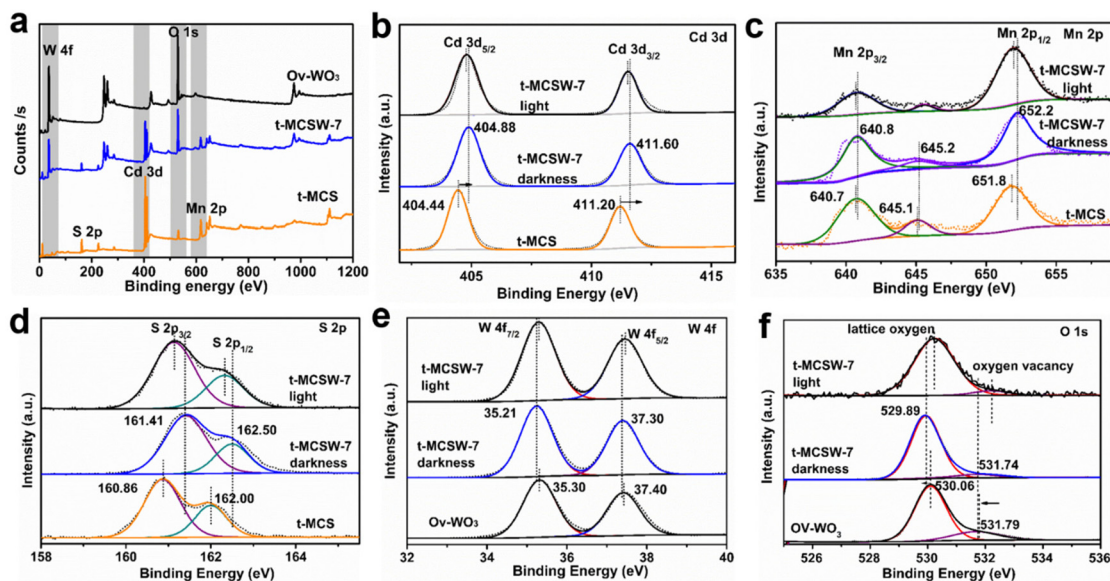


Fig. 3 XPS spectra of t-MCS, Ov-WO₃ and t-MCSW-7: (a) survey spectra and the corresponding high-resolution spectra of Cd 3d (b), Mn 2p (c), S 2p (d), W 4f (e) and O 1s (f) under dark conditions and light irradiation.

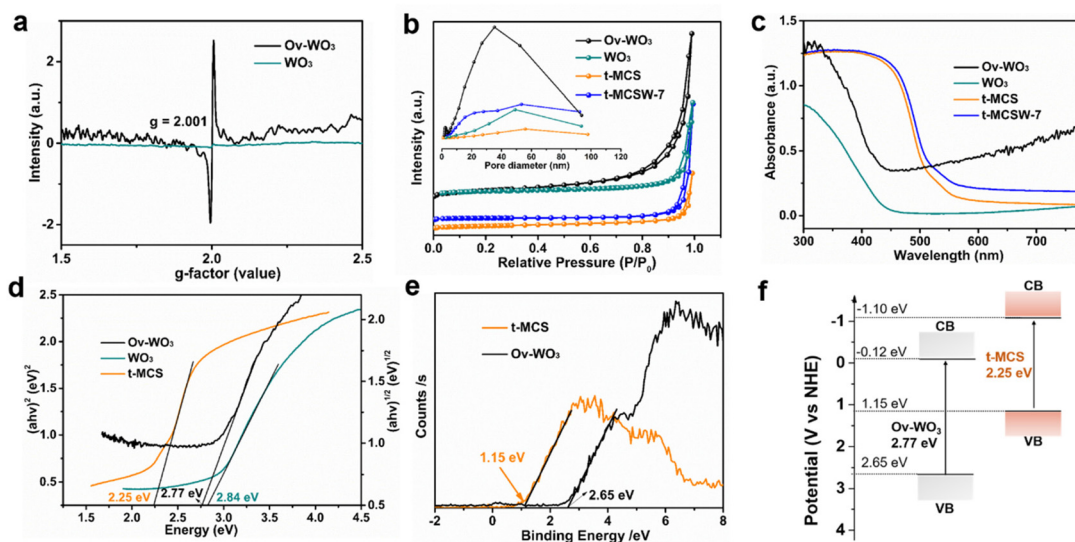


Fig. 4 (a) EPR spectra of samples, (b) BET isotherms (inset shows pore size distribution curves), (c) UV-vis DRS of samples, (d) the energy gaps, (e) XPS VB spectra, and (f) band gap diagram of t-MCS and Ov-WO₃.

t-MCSW-7 material demonstrates excellent photo-response. These results suggest that the absorption efficiency of t-MCSW-7 is boosted after loading Ov-WO₃, which is more conducive to the improvement of hydrogen evolution.

The corresponding bandgaps of the samples can be calculated using the following formula:

$$\alpha h\nu = A(h\nu - E_g)^{n/2}, \quad (1)$$

where $n = 1$ for a direct energy gap semiconductor and $n = 4$ for an indirect bandgap semiconductor.^{19,50,51} The t-MCS is a

direct semiconductor, whereas Ov-WO₃ is an indirect bandgap semiconductor, according to the literature.³⁶ It is observed that the construction of the vacancy narrows the energy gap of pure WO₃. The optical intrinsic bandgaps of t-MCS and Ov-WO₃ are measured to be 2.25 eV and 2.77 eV, respectively (Fig. 4d), which are in agreement with the theoretical calculation (Fig. S6†).^{36,44,45} The excellent photocatalysts need a reasonable CB potential and VB potential in addition to having an appropriate bandgap energy.³⁵ Furthermore, the VB potentials of the t-MCS and Ov-WO₃ are 1.15 eV and 2.65 eV attained from XPS VB spectra, respectively (Fig. 4e). Based on

the equation $E_g = E_{VB} - E_{CB}$, the CB potentials of t-MCS and Ov-WO₃ were calculated to be -1.10 eV and -0.12 eV, respectively, which is consistent with the Mott-Schottky curve results (Fig. S7†).⁴⁴ The schematic diagram of the corresponding bandgap, valence, and conduction band positions is shown in Fig. 4f for further analysis of the mechanism.

3.3. Photocatalytic hydrogen activity

The photocatalytic hydrogen evolution performance of the samples was evaluated using Na₂S/Na₂SO₃ sacrificial agents under visible light. Fig. 5a and Fig. S8† illustrate the photocatalytic hydrogen evolution activity of a series of nanotwin Mn_xCd_{1-x}S samples. Single CdS presents a comparatively low H₂ rate of 11.8 mmol g⁻¹ h⁻¹, which can be credited to the quick recombination of photo-generated carriers.²¹ Pure MnS also demonstrates a negligible H₂ rate. With the increase in Mn²⁺, the rate of hydrogen evolution of Mn_xCd_{1-x}S increases gradually and reaches a maximum of 48.8 mmol g⁻¹ h⁻¹ for t-MCS.

Fig. 5b and c depicts the hydrogen performance of t-Mn_{0.5}Cd_{0.5}S/Ov-WO₃-x (t-MCSW-x) loaded with different amounts of Ov-WO₃. It can be seen that the hydrogen production activity shows a volcanic trend. Obviously, the activity of t-MCSW-x is related to the content of Ov-WO₃. When an

introduction amount of Ov-WO₃ is 7 wt%, t-MCSW-7 achieves maximum hydrogen evolution activity at 194.2 mmol g⁻¹ h⁻¹, which is 4-fold higher compared with t-MCS (48.8 mmol g⁻¹ h⁻¹). Meanwhile, it can be observed that the hydrogen rate of t-MCSW-7 is significantly higher than that of t-MCS/WO₃-7 (physical mixture, 96.7 mmol g⁻¹ h⁻¹). The results indicate that the photocatalytic activity is not only closely related to the formation of homojunctions and heterojunctions but also attributed to the content of oxygen vacancies. An appropriate amount of oxygen vacancies can serve as electron or hole capture centers to suppress carrier recombination, but excessive oxygen vacancies can serve as recombination centers for carriers. Also, the hydrogen evolution rates of different samples at $\lambda > 510$ nm are shown in Fig. S9.† Obviously, the hydrogen rate of t-MCSW-7 is significantly higher than that of pristine t-MCS, indicating that the modification of Ov-WO₃ effectively broadens the spectral absorption range at 510–800 nm. In addition, t-MCSW-7 shows better activity compared with recently reported Mn_xCd_{1-x}S-based materials in photocatalytic hydrogen evolution (Fig. 5c, Table S2†). Furthermore, as illustrated in Fig. 5e, the AQY values of t-MCSW-7 are 29.14% at 420 nm, 20.63% at 450 nm, 7.81% at 520 nm, and 3.51% at 600 nm, respectively. Its AQY trend corresponds well with its optical absorption, indicating that

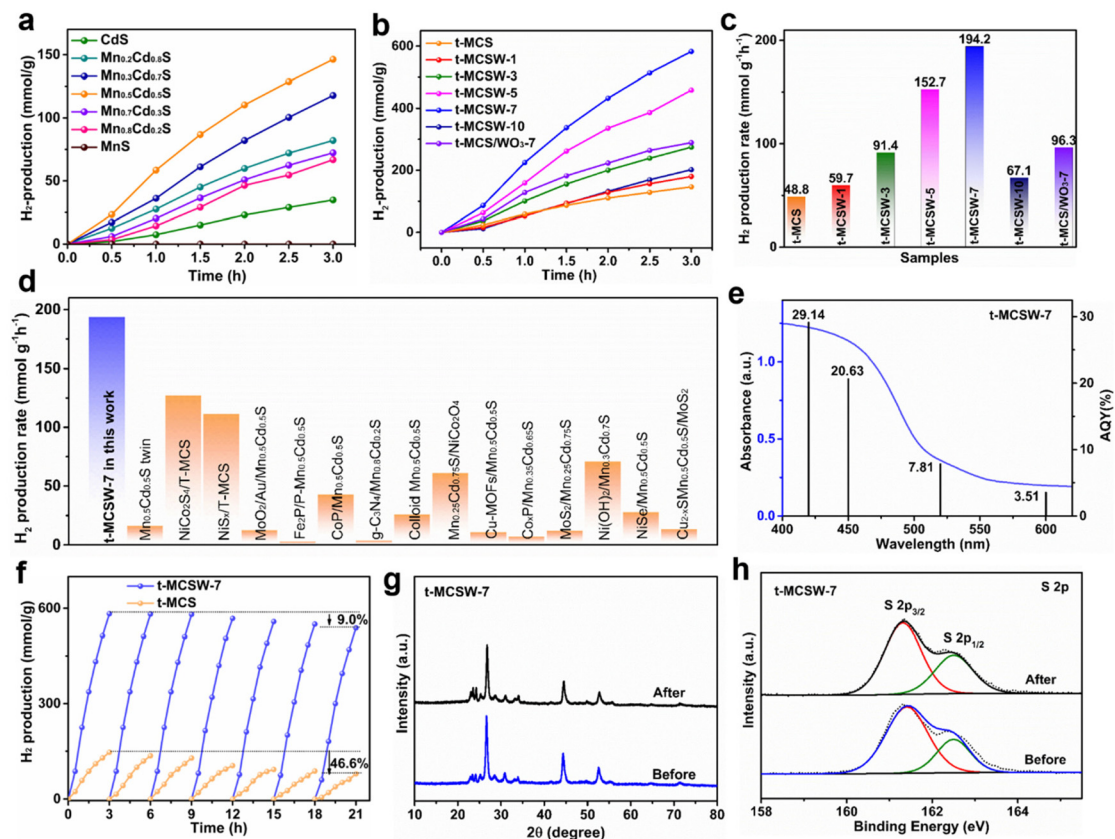


Fig. 5 The amount of hydrogen evolution of nanotwin Mn_xCd_{1-x}S materials (a) and (b) t-MCSW-x, (c) hydrogen evolution rate of t-MCSW-x, (d) the compared photocatalytic hydrogen rate of Mn_xCd_{1-x}S-based photocatalysts, (e) apparent quantum yield of t-MCSW-7, (f) the stability experiment of t-MCSW-7, (g) XRD patterns and (h) the XPS S 2p spectrum before and after cycling.

t-MCSW-7 promotes the progress of the photocatalytic reaction.⁵² Excellent photocatalysts not only have high catalytic activity but also should have good stability performance. As shown in Fig. 5f, the stability of t-MCSW-7 and t-MCS was assessed with long-term cycling experiments. After seven cycles of photocatalytic reaction, compared to the pristine t-MCS, the hydrogen production activity of t-MCSW-7 shows a slight decrease to about 9%, which suggests that the t-MCSW-7 heterojunction maintains high stability. The result is due to the introduction of Ov-WO₃ suppressing photo-corrosion of t-MCS and further improving photostability. In addition, the activity of t-MCSW-7 decreases after multiple cycles, which may be mainly due to the loss of the sample during centrifugation and recovery processes. XRD patterns and the S 2p XPS spectrum of t-MCSW-7 after the reaction further reveal the photostability (Fig. 5g and h). Compared to the XRD pattern before the reaction, diffraction peaks of t-MCSW-7 do not significantly change after cycling. S₀ was not detected in the S 2p XPS spectrum. The results suggest t-MCSW-7 shows excellent structural stability.

3.4. Photoelectrochemical properties analysis

To understand the dynamics of charge carrier separation, steady-state fluorescence and time-resolved fluorescence spectra of samples were collected at an excitation wavelength of 375 nm. Compared with the fluorescence signal of pure t-MCS, t-MCSW-7 exhibits a significant fluorescence quenching phenomenon (Fig. 6a), indicating a slow rate of charge carrier recombination in the composite material, demonstrating more effective charge separation, and leading to the improvement of photocatalytic hydrogen production.^{33,53–55} Meanwhile, the absolute fluorescence quantum yield (Φ_{PL}) of t-MCSW-7 (0.31%) is lower than that of single t-MCS (1.33%). Fig. 6b shows the fluorescence decay curves. The corresponding lifetimes obtained by double exponential fitting are

presented in Table S3.† τ_1 and τ_2 represent faster and slower decay times. The faster component is assigned to the direct formation of electrons and holes, while the slow component (τ_2) corresponds to an indirect formation of self-trapped excitons. The average lifetimes (τ_{ave}) of t-MCS, Ov-WO₃ and t-MCSW-7 are 8.226 ns, 7.806 ns, and 8.879 ns, respectively. The extension of the lifetime indicates that more photo-induced carriers participate in the catalytic reactions before recombination.⁵⁶ The results indicate that triple-phase junctions connected by homojunctions, heterojunctions and oxygen vacancies can synergistically suppress photogenerated carrier recombination in the bulk and surface, leading to a long lifetime.

Transient photocurrent responses of the samples are presented in Fig. 6c. t-MCSW-7 has a larger photocurrent intensity than single Ov-WO₃ sheets and pure t-MCS, respectively, indicating the effective separation of photogenerated electron-hole pairs. The EIS plots of different samples are presented in Fig. 6d. Normally, the diameter of a Nyquist plot reflects the magnitude of the charge transfer resistance of samples in the working electrode. Generally speaking, a smaller radius of a sample indicates a faster charge transfer rate. Compared to original Ov-WO₃ and t-MCS, the t-MCSW-7 material has a smaller radius, indicating the minimum charge carrier transfer resistance. The above results indicate that multiphase interfaces and oxygen vacancies in t-MCSW-7 effectively accelerate the separation and transfer of photogenerated carriers.

To investigate the charge transfer mechanism, ESR experiments were performed with spin-trapping reagents. Samples were dispersed in DMPO solutions to identify radical intermediates ($\cdot\text{OH}$ and $\cdot\text{O}_2^-$), respectively.^{57–59} $\cdot\text{OH}$ radicals and $\cdot\text{O}_2^-$ radicals were generated at 2.34 eV ($\text{H}_2\text{O} + h\nu_{\text{VB}} \rightarrow \cdot\text{OH} + \text{H}^+$) and -0.33 eV ($\text{O}_2 + e_{\text{CB}} \rightarrow \cdot\text{O}_2^-$) vs. NHE, respectively.⁶⁰ As illustrated in Fig. 7a, after 10 min of irradiation, ESR signals exhibit four characteristic peaks of DMPO- $\cdot\text{OH}$ for Ov-WO₃ and t-MCSW-7, suggesting that photogenerated holes in the samples react at a higher VB than the potential of H₂O/ $\cdot\text{OH}$ pairs. On the other hand, as shown in Fig. 7b, DMPO- $\cdot\text{O}_2^-$ is identified with six characteristic ESR signals for t-MCS and t-MCSW-7, indicating electrons reacted at a lower CB than the potential of the O₂/ $\cdot\text{O}_2^-$ couple. Comparing with Fig. 4f, the VB of pure Ov-WO₃ (2.65 eV) is positive compared to the poten-

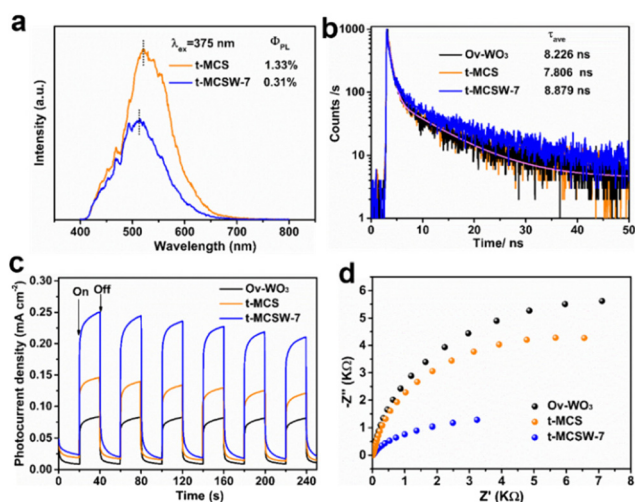


Fig. 6 (a) Steady-state fluorescence spectra (PL), (b) Time-resolved photoluminescence spectra (TRPL), (c) transient photocurrent density curves, and (d) electrochemical impedance-Nyquist plots of samples.

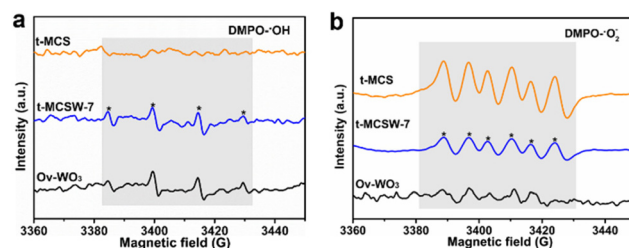


Fig. 7 ESR signal results of t-MCS, t-MCSW-7, and Ov-WO₃ samples for DMPO- $\cdot\text{OH}$ detection analysis in the aqueous solution and DMPO- $\cdot\text{O}_2^-$ detection in methanol after 10 min of irradiation.

tial of $\text{H}_2\text{O}/\text{OH}$ pairs, while the CB of single t-MCS (-1.10 eV) is more negative compared to the potential of the O_2/O_2^- couple, and thus, $\text{DMPO}\cdot\text{OH}$ and $\text{DMPO}\cdot\text{O}_2^-$ signals were detected, respectively. For t-MCSW-7, both $\text{DMPO}\cdot\text{OH}$ and $\text{DMPO}\cdot\text{O}_2^-$ signals are clearly observed. The strong $\cdot\text{O}_2^-$ and $\cdot\text{OH}$ signals verify the mechanism that the t-MCSW-7 heterojunction conforms with the S-scheme band structure, not the conventional Type-II.

The work function (Φ) is the crucial indicator for elucidating the charge transfer pathway between two semiconductors.^{8,61–63} As illustrated in Fig. 8a and b, the electrostatic potentials and optimal models of t-MCS and Ov-WO₃ further clarify the carrier migrating process through theoretical simulation. t-MCS (002) and Ov-WO₃ (200) have a computed work function of 3.434 eV and 4.061 eV, respectively. It is clear from the results that the Fermi level (E_f) of Ov-WO₃ is more negative than that of t-MCS. The electrons on t-MCS will flow to Ov-WO₃ when t-MCS and Ov-WO₃ are closely combined until the Fermi levels are equivalent.^{27,62} This creates a potential difference between t-MCS and Ov-WO₃, with positive charges accumulating on t-MCS and negative charges on Ov-WO₃. Therefore, an internal electric field is formed at the heterojunction interface between t-MCS and Ov-WO₃. The direc-

tion of the internal electric field is from t-MCS to Ov-WO₃. At the same time, in *in situ* XPS spectra, electrons drift from t-MCS to Ov-WO₃ in the composite under dark conditions, while all peaks for t-MCSW-7 are observed to move in the opposite direction compared with that under dark conditions under irradiation. Their results are consistent with the ESR analysis, which indicates that t-MCS and Ov-WO₃ form an S-scheme system.

Based on the above results, the photocatalytic charge transfer mechanism diagram of t-MCS/Ov-WO₃ (t-MCSW) is illustrated in Fig. 8c. After the two semiconductors come into contact, an internal electric field is formed at the heterojunction interface, and the band edge of t-MCS bends upwards due to the loss of electrons, while the band edge of Ov-WO₃ bends downwards because of the gaining of electrons. Under visible light, photoinduced electrons are excited from the VB to the CB of t-MCS and Ov-WO₃, respectively. Photogenerated holes remain in the VB. Within t-MCS, driven by the homojunction interface, photogenerated electrons are transferred from the CB of the WZ phase to the CB of the ZB phase.^{32,33} Driven by the built-in electric field and energy band bending of the heterojunction interface,^{44,56} electrons enriched in oxygen vacancies of Ov-WO₃ are transferred to the VB of t-MCS, so the

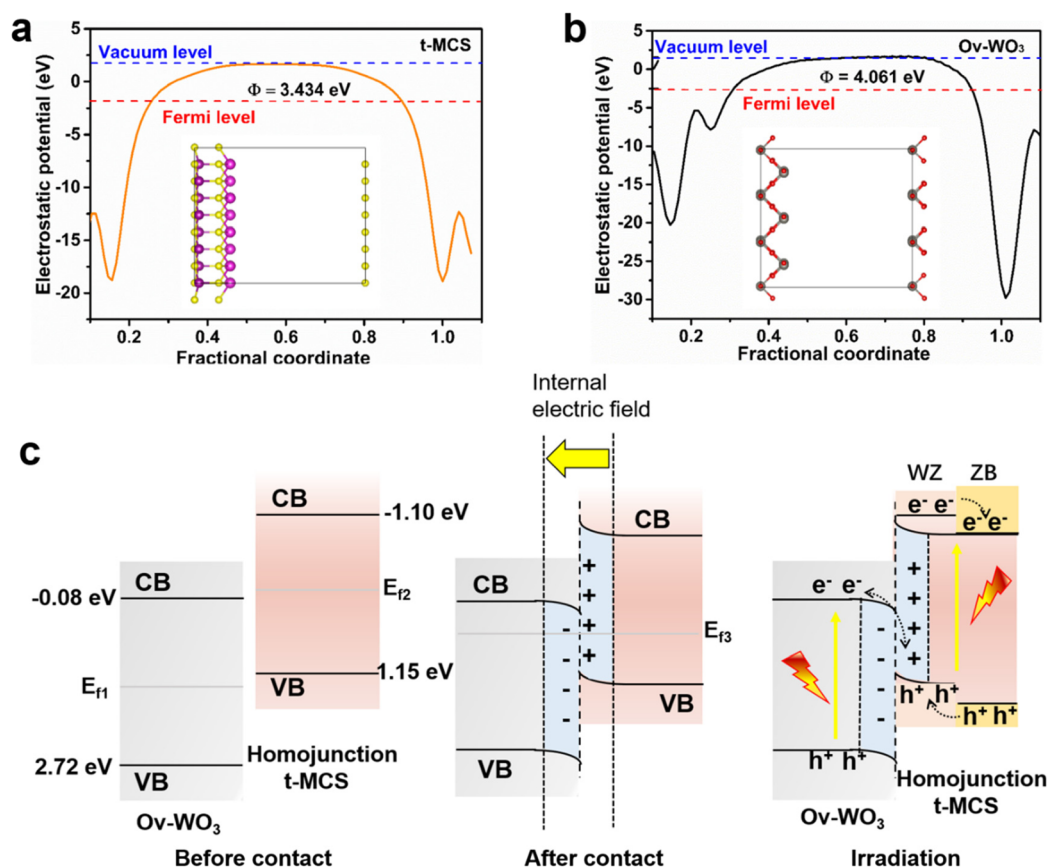


Fig. 8 Electrostatic potentials of t-MCS (002) (a) and Ov-WO₃ (200) (b) planes (inset shows the structural model; the purple, deep purple, yellow, red and gray spheres represent Cd, Mn, S, O and W atoms, respectively), (c) the proposed S-scheme carrier transfer mechanism over the t-MCSW-7 heterostructure.

electrons in the CB of t-MCS and holes in the VB of Ov-WO₃ are efficiently separated. Finally, the electrons on the CB of the ZB phase of t-MCS reduce H⁺ to H₂, and holes on the VB of Ov-WO₃ oxidize the sacrificial agents. Therefore, the heterojunction endows the photoinduced electrons and holes with a stronger redox ability to be retained, contributing to a more significant photocatalytic hydrogen production performance for the t-MCSW-7 composite.

4. Conclusions

In summary, a novel Mn_{0.5}Cd_{0.5}S/Ov-WO₃ (t-MCSW) composite with nanotwin Mn_{0.5}Cd_{0.5}S and Ov-WO₃ nanosheets of rich oxygen vacancies was prepared using the hydrothermal method for the first time. The presence of homojunctions and heterojunctions enhances the separation of photogenerated charge carriers. Meanwhile, the surface oxygen vacancies in Ov-WO₃ nanosheets act as hole-capture centers and sites for oxidizing the sacrificial agent, which further improves the photostability of t-MCSW-7. In addition, the S-scheme heterojunction of t-MCSW provides a stronger reduction potential. The hydrogen evolution rate of t-MCSW-7 reaches 194.2 mmol g⁻¹ h⁻¹ in the Na₂S/Na₂SO₃ sacrificial agent environment, which is four times higher than that of a single t-MCS (48.8 mmol g⁻¹ h⁻¹). Cycling stability performance of t-MCSW-7 has been greatly improved due to the export of photogenerated holes resulting in the suppression of photo-corrosion of the materials. This article provides a novel idea for high-performance photocatalysts.

Conflicts of interest

There are no conflicts to declare.

Acknowledgements

We sincerely thank the Liaocheng University Doctoral Initial Fund (318052011) for financial support.

References

- Z. Li, W. Li, L. Zhai, C. Chen, J. Zhang and Z. Wang, *J. Colloid Interface Sci.*, 2023, **646**, 834–843.
- X. Ma, W. Li, H. Li, M. Dong, L. Geng, T. Wang, H. Zhou, Y. Li and M. Li, *J. Colloid Interface Sci.*, 2023, **639**, 87–95.
- Y. Shi, L. Li, Z. Xu, X. Qin, Y. Cai, W. Zhang, W. Shi, X. Du and F. Guo, *J. Colloid Interface Sci.*, 2023, **630**, 274–285.
- T. He, W. Zhen, Y. Chen, Y. Guo, Z. Li, N. Huang, Z. Li, R. Liu, Y. Liu, X. Lian, C. Xue, T. C. Sum, W. Chen and D. Jiang, *Nat. Commun.*, 2023, **14**, 329–340.
- H. Li, J. J. M. Vequizo, T. Hisatomi, M. Nakabayashi, J. Xiao, X. Tao, Z. Pan, W. Li, S. Chen, Z. Wang, N. Shibata, A. Yamakata, T. Takata and K. Domen, *EES Catal.*, 2023, **1**, 26–35.
- X. Zheng, Y. Song, Y. Liu, J. Li, Y. Yang, D. Wu, W. Liu, Y. Shen and X. Tian, *Small*, 2023, **19**, 2207623–2207634.
- X. Tao, Y. Zhao, S. Wang, C. Li and R. Li, *Chem. Soc. Rev.*, 2022, **51**, 3561–3608.
- Z. Li, Y. Yang, K. Dai, J. Zhang and L. Lu, *Appl. Surf. Sci.*, 2019, **469**, 505–513.
- C. Li, G. Ding, X. Liu, P. Huo, Y. Yan, Y. Yan and G. Liao, *Chem. Eng. J.*, 2022, **435**, 134740–134749.
- D. Huang, M. Wen, C. Zhou, Z. Li, M. Cheng, S. Chen, W. Xue, L. Lei, Y. Yang, W. Xiong and W. Wang, *Appl. Catal., B*, 2020, **267**, 118651–118665.
- F. Kang, C. Shi, Y. Zhu, M. Eqi, J. Shi, M. Teng, Z. Huang, C. Si, F. Jiang and J. Hu, *J. Energy Chem.*, 2023, **79**, 158–167.
- J. Song, H. Zhao, R. Sun, X. Li and D. Sun, *Energy Environ. Sci.*, 2017, **10**, 225–235.
- H. Zhao, X. Zhao, L. Shen, H. Liu and X. Li, *Chem. Eng. J.*, 2023, **470**, 143925–143935.
- L. Li, G. Liu, S. Qi, X. Liu, L. Gu, Y. Lou, J. Chen and Y. Zhao, *J. Mater. Chem. A*, 2018, **6**, 23683–23689.
- X. Liu, Q. Liu, P. Wang, Y. Liu, B. Huang, E. A. Rozhkova, Q. Zhang, Z. Wang, Y. Dai and J. Lu, *Chem. Eng. J.*, 2018, **337**, 480–487.
- K. Ikeue, S. Shiiba and M. Machida, *Chem. Mater.*, 2009, **22**, 743–745.
- Y. Sun, Y. Li, J. He, L. Chen, H. Ji, Z. Qin and T. Su, *Chin. J. Struct. Chem.*, 2023, **42**, 100145–100155.
- J. Yan and L. Shi, *Int. J. Energy Res.*, 2022, **46**, 8218–8228.
- M. Xiong, Y. Qin, B. Chai, J. Yan, G. Fan, F. Xu, C. Wang and G. Song, *Chem. Eng. J.*, 2022, **428**, 131069–131079.
- H. Peng, Y. Du, X. Zheng and J. Wen, *Int. J. Hydrogen Energy*, 2022, **47**, 9925–9933.
- J. Zhang, C. Cheng, F. Xing, C. Chen and C. Huang, *Chem. Eng. J.*, 2021, **414**, 129157–129163.
- M. Luo, G. Jiang, M. Yu, Y. Yan, Z. Qin, Y. Li and Q. Zhang, *J. Mater. Sci. Technol.*, 2023, **161**, 220–232.
- Y. Yu, W. Yan, X. Wang, P. Li, W. Gao, H. Zou, S. Wu and K. Ding, *Adv. Mater.*, 2018, **30**, 1705060–1705068.
- C. Wang, X. Ma, Z. Fu, X. Hu, J. Fan and E. Liu, *J. Colloid Interface Sci.*, 2021, **592**, 66–76.
- C. Cheng, J. Zhang, B. Zhu, G. Liang, L. Zhang and J. Yu, *Angew. Chem., Int. Ed.*, 2023, **62**, 202218688–202218696.
- L. Zhang, J. Zhang, H. Yu and J. Yu, *Adv. Mater.*, 2022, **34**, 2107668–2107684.
- Z. Zhang, M. Wang, Z. Chi, W. Li, H. Yu, N. Yang and H. Yu, *Appl. Catal., B*, 2022, **313**, 121426–121438.
- X. Wu, G. Chen, J. Wang, J. Li and G. Wang, *Acta Phys.-Chim. Sin.*, 2023, **39**, 2212016–2212036.
- K. Zhang, Y. Li, S. Yuan, L. Zhang and Q. Wang, *Acta Phys.-Chim. Sin.*, 2023, **39**, 2212010–2212028.
- L. Yuan, C. Zhang, Y. Zou, T. Bao, J. Wang, C. Tang, A. Du, C. Yu and C. Liu, *Adv. Funct. Mater.*, 2023, **33**, 2214627–2214637.
- B. Su, M. Zheng, W. Lin, X. Lu, D. Luan, S. Wang and X. Lou, *Adv. Energy Mater.*, 2023, **13**, 2203290–2203299.

- 32 Y. Zhao, W. Xue, W. Sun, H. Chen, X. Li, X. Zu, S. Li and X. Xiang, *Int. J. Hydrogen Energy*, 2023, **48**, 31161–31171.
- 33 Z. Wang, M. Li, J. Li, Y. Ma, J. Fan and E. Liu, *J. Environ. Chem. Eng.*, 2022, **10**, 107375–107384.
- 34 Y. Liu, L. Wang, H. Lv, X. Wu, X. Xing and S. Song, *Appl. Surf. Sci.*, 2021, **541**, 148582–148592.
- 35 Z. Zhao, Z. Wang, J. Zhang, C. Shao, K. Dai, K. Fan and C. Liang, *Adv. Funct. Mater.*, 2023, 2214470–2214482.
- 36 T. Hu, P. Li, J. Zhang, C. Liang and K. Dai, *Appl. Surf. Sci.*, 2018, **442**, 20–29.
- 37 S. Li, J. Wang, Y. Xia, P. Li, Y. Wu, K. Yang, Y. Song, S. Jiang, T. Zhang and B. Li, *Chem. Eng. J.*, 2021, **417**, 129298–129302.
- 38 T. Liu, Y. Wang, P. Shan, Y. Chen, X. Zhao, W. Tian, Y. Zhang, R. Feng, H. Yuan and H. Cui, *Appl. Surf. Sci.*, 2021, **564**, 150117–150125.
- 39 M. Zhao, S. Liu, D. Chen, S. Zhang, S. A. C. Carabineiro and K. Lv, *Chin. J. Catal.*, 2022, **43**, 2615–2624.
- 40 J. Chen, X. Xiao, Y. Wang and Z. Ye, *J. Alloys Compd.*, 2019, **777**, 325–334.
- 41 S. Cao and H. Chen, *J. Alloys Compd.*, 2017, **702**, 644–648.
- 42 G. Chen, Z. Zhou, B. Li, X. Lin, C. Yang, Y. Fang, W. Lin, Y. Hou, G. Zhang and S. Wang, *J. Environ. Sci.*, 2023, DOI: [10.1016/j.jes.2023.05.028](https://doi.org/10.1016/j.jes.2023.05.028).
- 43 X. Zhang, W. Hao, C.-S. Tsang, M. Liu, G. S. Hwang and L. Y. S. Lee, *ACS Appl. Energy Mater.*, 2019, **2**, 8792–8800.
- 44 T. Feng, H. Li, R. Gao, G. Su, W. Wang, B. Dong and L. Cao, *ChemSusChem*, 2022, **15**, 202200288–202200298.
- 45 Y. Liu, J. Yan, D. Liu and L. Shi, *J. Alloys Compd.*, 2023, **938**, 168545–168554.
- 46 X. He, D. Zeng, Y. Liu, Q. Chen, J. Yang, R. Gao, T. Fujita and Y. Wei, *J. Colloid Interface Sci.*, 2022, **625**, 859–870.
- 47 H. Liu, Z. Xu, Z. Zhang and D. Ao, *Appl. Catal., A*, 2016, **518**, 150–157.
- 48 J. Huang, Z. Feng, Z. Chen, X. Li and X. Ma, *J. Inorg. Mater.*, 2023, **38**, 63–69.
- 49 H. He, H. Chen, P. Ning, J. Liang, X. Yao, Y. Gao, P. Byambatsogt, L. Qin, Y. Huang and D. Chen, *Renewable Energy*, 2022, **194**, 868–874.
- 50 R. Shen, L. Zhang, X. Chen, M. Jaroniec, N. Li and X. Li, *Appl. Catal., B*, 2022, **266**, 118619–118628.
- 51 J. Yan, Y. Wang and L. Shi, *Dalton Trans.*, 2022, **51**, 10279–10289.
- 52 Y. Cao, G. Wang, Q. Ma and Z. Jin, *Mol. Catal.*, 2020, **492**, 111001–111010.
- 53 X. Zhang, M. Gao, L. Qiu, W. Yang and Y. Yu, *Chem. Eng. J.*, 2023, **465**, 142747–142756.
- 54 P. Zhang, X. Zhan, L. Xu, X. Fu, T. Zheng, X. Yang, Q. Xu, D. Wang, D. Qi, T. Sun and J. Jiang, *J. Mater. Chem. A*, 2021, **9**, 26286–26297.
- 55 P. Zhang, T. Sun, L. Xu, Q. Xu, D. Wang, W. Liu, T. Zheng, G. Yang and J. Jiang, *ACS Sustainable Chem. Eng.*, 2023, **11**, 343–352.
- 56 R. K. Chava, N. Son and M. Kang, *J. Colloid Interface Sci.*, 2022, **627**, 247–260.
- 57 M. Humayun, H. Ullah, J. Cao, W. Pi, Y. Yuan, S. Ali, A. A. Tahir, P. Yue, A. Khan, Z. Zheng, Q. Fu and W. Luo, *Nano-Micro Lett.*, 2019, **12**, 7–25.
- 58 M. Hao, D. Wei and Z. Li, *Energy Fuels*, 2022, **36**, 11524–11531.
- 59 B. Su, H. Huang, Z. Ding, M. B. Roeffaers, S. Wang and J. Long, *J. Mater. Sci. Technol.*, 2022, **124**, 164–170.
- 60 D. Kim and K. Yong, *Appl. Catal., B*, 2021, **282**, 119538–119548.
- 61 X. Ke, K. Dai, G. Zhu, J. Zhang and C. Liang, *Appl. Surf. Sci.*, 2019, **481**, 669–677.
- 62 S. Wang, B. Zhu, M. Liu, L. Zhang, J. Yu and M. Zhou, *Appl. Catal., B*, 2019, **243**, 19–26.
- 63 Y. Wang, C. Yang, Y. Zhang, L. Guo, Y. Wang, G. Gao, F. Fu, B. Xu and D. Wang, *Int. J. Hydrogen Energy*, 2022, **47**, 9566–9578.